



# High-temperature failure and microstructural investigation of wire-arc additive manufactured Rene 41

William Sean James<sup>1</sup> · Supriyo Ganguly<sup>1</sup> · Goncalo Pardal<sup>1</sup>

Received: 9 September 2022 / Accepted: 11 January 2023  
© The Author(s) 2023

## Abstract

In developing a wire-arc plasma direct energy deposition process for creep-resistant alloys used in high-speed flight applications, structures were built from nickel-based superalloy Rene 41. Samples of additive manufacturing (AM) material were analysed for their microstructural and mechanical properties, in both as-deposited (AD) and heat-treated (HT) conditions. Tensile specimens were tested at room temperature, 538, 760, and 1000 °C. Macroscopically, large columnar grains made up of a typical dendritic structure were observed. Microscopically, significant segregation of heavier elements, grain boundary precipitates, and secondary phases were observed, with key differences observed in HT material. There was a clear distinction between failure modes at different testing temperatures and between AD and HT variants. A fractographic investigation found a progressive move from brittle to ductile fracture with increasing testing temperature in both AD and HT conditions, as well as microstructural features which support this observation.

**Keywords** Additive manufacturing · Direct energy deposition · Mechanical properties · Fractography · Microstructure · Rene 41

## Abbreviations

RE41 Rene 41  
AD As-deposited  
HT Heat-treated

## 1 Introduction

The use of a wire-arc-based direct energy deposition (DED) process for the manufacture of creep-resistant superalloys is a relatively new area of study, and the effect of DED on material performance at high temperatures is little understood. The DED process where an electrical arc is used to melt and deposit a metal wire feedstock is also known as wire + arc additive manufacturing (WAAM). WAAM has a proven capability for the deposition of a range of different alloys and metals. Williams et al. describe how the process can be used to build components in titanium, aluminium, and steel alloys [1], and Marinelli et al. had success with depositing refractory components, using a tungsten inert gas

(TIG) process to deposit high-purity tungsten [2]. In addition to the above, Xu et al. deposited creep-resistant alloys such as nickel-based superalloy Inconel 718 [3], and James et al. deposited Rene 41 (RE41) and cobalt-based Haynes 188 [4]. WAAM can take advantage of a variety of different deposition processes such as TIG, MIG, and plasma transferred arcs (PTA). WAAM is currently a developing technology in the early stages of commercialising.

In developing the WAAM process for creep-resistant alloys used in high-speed flight environments, James et al. deposited RE41, amongst other superalloys, using a PTA WAAM process in an oxygen-controlled environment. They found that RE41 was the most suitable alloy, of those studied, for WAAM and the high-speed flight application [4]. This study goes on to continue this work, in investigating the high-temperature properties and the effect of post-deposition heat treatment as a method to return the performance of RE41 to the wrought strength.

RE41 is a Ni-based, Cr, Co superalloy with applications in aerospace components, where high strength is required at operating temperatures between 650 and 980 °C, such as afterburner and gas turbine parts [5]. Wile gives more specific high-profile applications of RE41, such as its use in the skin on the mercury space capsule and its application in components for the nuclear power industry [6].

✉ William Sean James  
w.james@cranfield.ac.uk

<sup>1</sup> Welding and Additive Manufacturing Centre, Cranfield University, Cranfield MK43 0AL, Bedfordshire, UK

There is little published research on specifically wire-based DED of RE41 using PTA. The work presented in this paper follows on from the work of James et al., in which samples of several alloys including RE41 were deposited, and testing in room-temperature (RT) conditions, they found a mismatch in performance compared with wrought material [4]. There is, however, more literature published on the deposition of RE41 using laser-based AM. Li et al. used a laser melting deposition (LMD) process to manufacture RE41 specimens for analysis. They found LMD RE41 had a fine rapid directionally solidified granular structure. They also found that the standard heat treatment for RE41 was not suitable for LMD built RE41, due to the extensive precipitation of  $\gamma'$  particles, the primary strengthening phase, which resulted in high hardness and ductility and ultimately worked to decrease the strength of the alloy compared with AD material [7]. In another study by Li and Wang, RE41 was again deposited using LMD and underwent mechanical testing. When testing at 800 °C, RE41 was described as having excellent performance with an ultimate tensile strength (UTS) of 855 MPa and a yield strength (YS) of 682 MPa. They also found that the fracture surfaces contained secondary cracking and a local stepwise fracture surface [8].

Atabay et al. investigated RE41 deposited by a laser powder bed fusion (LPBF) process. Much like Li et al. they found that RE41 fabricated by LPBF had a fine columnar grain structure. Atabay et al. also observed  $\gamma'$  precipitation after heat treatment using transmission electron microscopy (TEM) but did not observe the precipitates in AD condition. When they were observed after heat treatment they were considerably smaller than suggested in literature. They also observed the formation of Mo-rich carbides at the grain boundaries. Specimens tested at RT achieved a UTS and YS of approx. 1165 and 857 MPa respectively. The fractographic analysis revealed samples fractured in a ductile manner. In contrast to Li et al., Atabay et al. found that the standard heat treatment was satisfactory to meet their requirement [9][9].

The intended outcome of this study is to understand the microstructural effects a plasma WAAM process has on RE41 and how to maximise the performance for use in a high-speed flight environment, where external structures could reach service temperatures as high as 1000 K and 1200 + K for components in the propulsion flow path. The choice to select a plasma process was made with a view to building final components; in this respect, it is important for heat input and wire feeding to be independently adjustable.

### 1.1 Strengthening mechanisms of this alloy

The phases seen throughout superalloys are dependent on their composition and are described by Donachie and Donachie in their book, *Superalloys: A Technical Guide*.

Most superalloys have an austenitic face-centred cubic (fcc) phase known as the  $\gamma$  phase and consist of several other secondary phases. Carbides are a secondary phase and take the form of MC,  $M_6C$ ,  $M_{23}C_6$ , and  $M_7C_3$ , where 'M' represents the metallic element. Other secondary phases consist of intermetallic compounds, which commonly include  $\gamma'$  fcc phase  $Ni_3(Al,Ti)$ ,  $\gamma''$  body-centred tetragonal (bct) phase  $Ni_3Nb$ ,  $\eta$  hexagonal ordered phase  $Ni_3Ti$ , and  $\delta$  phase orthorhombic  $Ni_3Nb$ . In most superalloys given the right conditions, undesirable phases can form, which can harm the performance if present in larger amounts. These typically include topologically close-packed (tcp) phases:  $\mu$   $Co_2W_6/(Fe,Co)_7(Mo,W)_6$ , Laves phase  $A_2B$  type where 'A' and 'B' represent metallic elements, and  $\sigma$  can include more complex intermetallic phases [10].

Schwartz et al. describe the basic metallurgy and strengthening mechanism of RE41 when they investigated the use of the alloy in extrusion dies; the alloy is a precipitation strengthened Ni-based superalloy with a fcc austenitic matrix; RE41 also contains a large amount of Cr, Co, and Mo. The main strengthening phase is  $\gamma'$   $Ni_3(Al,Ti)$  [11]. More historic research by Kaufman describes the formable phases in RE41 in more detail.  $Ni_3Al$  and  $Ni_3Ti$  form fine uniform particles at 760 °C which are coarser at higher temperatures.  $Ni_3Ti$  appears fine below 760 °C and acicular above 760 °C.  $Ni_3Al$  appears coarse and curved and is seen in larger amounts at grain boundaries.  $\delta$  phases are not seen generally due to Cr and Mo being tied up in the carbides. Laves phase can form where C is less than 0.05% and Al less than 1% at 815 °C [12]. Weisenberg and Morris describe how the main strengthening phase,  $\gamma'$ , forms as the alloy ages,  $\gamma'$  is mostly prevalent between 760 and 1010 °C, and the particles increase in size with temperature until dissolved at around 1050 °C. The phases present in the alloy vary with exposure to temperature [13]. The characterisation of RE41 by Collins and Quigg gives an estimation as to the probability of certain phases being present in the alloy. Of the formable phases, the MC-type carbide is the most dominant at lower temperatures until 816 °C and again at higher temperatures between 1150 and 1200 °C. The tcp  $\mu$  phase is most stable around 930 °C.  $M_6C$  is most dominant between 980 and 1150 °C. The amount of  $M_{23}C_6$  increases with temperature until it reaches a maximum at 870 °C and starts to become unstable at 980 °C. The amount of  $\sigma$  phase also increases with temperature, reaching a maximum at 980 °C and becomes unstable thereafter [14]. An interpretation of the phases formable with aging temperature is presented in Fig. 1.

In the more recent study using LPBF, Atabay et al. found that of the formable carbides observed, MC was rich in Mo and Ti,  $M_6C$  was rich in Mo and Co, and  $M_{23}C_6$  was found to be rich in Cr [9].

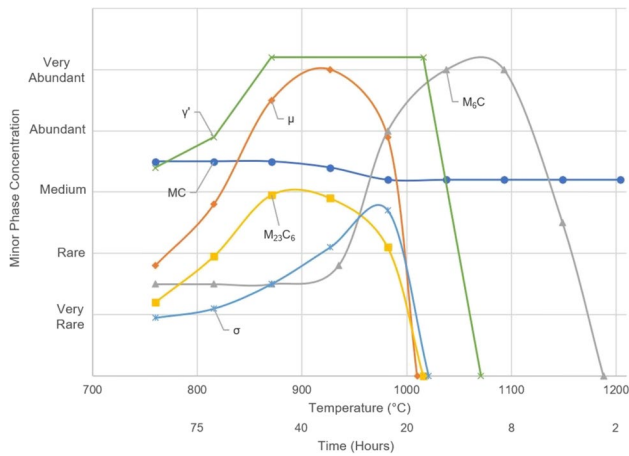


Fig. 1 Minor phase concentration as a function of aging temperature. Adapted from [14] and [13]

## 2 Experimental method

### 2.1 Manufacturing process

A PTA WAAM process was used to produce samples for analysis from a commercially available 1-mm diameter RE41 wire. The WAAM system consisted of a water-cooled plasma welding torch and wire feeder mounted to a FANUC six-axis robotic arm, a part-rotator, and a gas enclosure. The enclosure provided an inert argon atmosphere for deposition, where the concentration of oxygen was controlled below 800 ppm with the use of an oxygen analyser. A symmetrical building process was used, meaning that material was deposited on both sides of the substrate plate, the main advantages of which are increased productivity and a reduction in residual stress, as described by Williams et al. [1]. Two wall structures measuring 350 × 110 × ~8 mm were deposited

Fig. 2 Experimental WAAM set-up

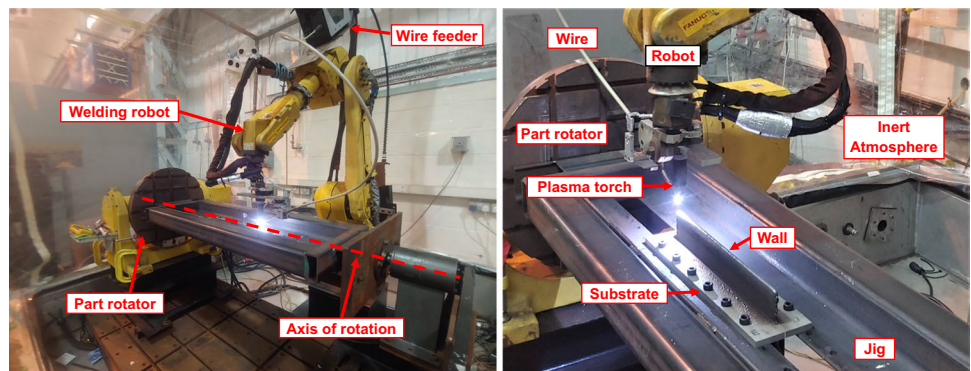


Table 1 Composition of RE41 wire (wt.%)

Ni	Cr	Co	Mo	Fe	Ti	Al	Nb	V	Si	C	Cu	Mn	B	S
53.7	18.9	10.2	9.08	2.72	3.20	1.64	0.12	0.12	0.09	0.07	0.04	0.03	0.004	<0.003

onto both sides of an Inconel 718 (IN718) substrate plate, using an arc current of 180 A, a wire-feed speed of 2.4 m/min, a torch travel speed of 0.36 m/min, a torch to work distance of 8 mm, and an interpass temperature of 170 °C after approx. 3 min of cooling time. A diagram of the set-up is shown in Fig. 2.

After deposition, samples were extracted and underwent the heat treatment recommended by Weisenberg and Morris for achieving maximum tensile performance. The heat treatment consisted of a solutionising treatment at 1065 °C for 4 h, after which the material was air-cooled to RT, followed by an aging treatment at 760 °C for 16 h and completed by air cooling to RT [13].

### 2.2 Composition

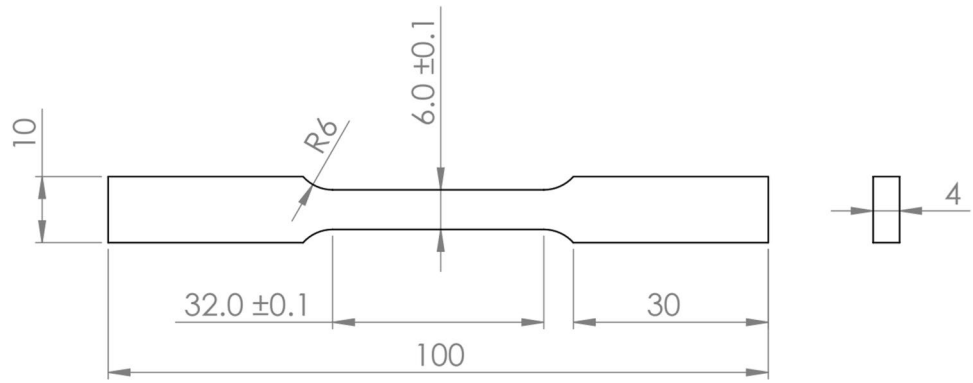
The wire feedstock underwent a chemical analysis to verify the alloy wire met the requirements for UNS N07041, the results of which are given in Table 1. To determine composition, the material was combusted and analysed using inductively coupled plasma–optical emission spectroscopy (ICP-OES).

### 2.3 Metallographic preparation and analysis

The WAAM walls were cut from the substrate plates and samples were extracted through both the wall height and length. Cross-sections were extracted and prepared for metallographic analysis following a procedure consisting of mounting then grinding and polishing successively, followed by etching. Samples were etched to reveal the microstructure using 3-g CuSO<sub>4</sub>, 80-ml HCl, and 20-ml absolute alcohol [7] swabbed for 30 s Figures 3 and 4.

The microstructure was analysed, using a Tescan VEGA 3 scanning electron microscope (SEM) and optically using

**Fig. 3** RT tensile testing coupon (dimensions in mm)



a Leica DM 2700 M microscope. To give an indication of composition, a semi-quantitative analysis of phases was conducted using the VEGA 3 SEM equipped with an Oxford Instruments X-Max 20-mm energy-dispersive spectrometry (EDS) detector. To determine the presence of lighter elements within the matrix, a Tescan Solaris X SEM was equipped with xenon plasma focused ion beam (FIB) and a TOFWERK time-of-flight secondary ion mass spectrometer (TOFSIMS).

The specimens were extracted in several locations across the WAAM walls; their locations in reference to the wall structure are shown in Fig. 5. From a total of four WAAM walls built in pairs, three walls were utilised for testing. After testing, the fracture surfaces of specimens in each category and condition were observed. The axis by which samples were observed is indicated going forwards with reference to Fig. 5, where BD is the build direction, WA is the wall axis, and TT is the through thickness.

To determine the dilution of the IN718 substrate into the RE41 matrix, samples containing both the deposited WAAM wall and a section of the substrate were extracted. The line scan function of the SEM-EDS system was then utilised to determine dilution of specific elements.

**2.4 Mechanical testing**

Samples were extracted from the WAAM walls and machined into coupons from the locations and in the

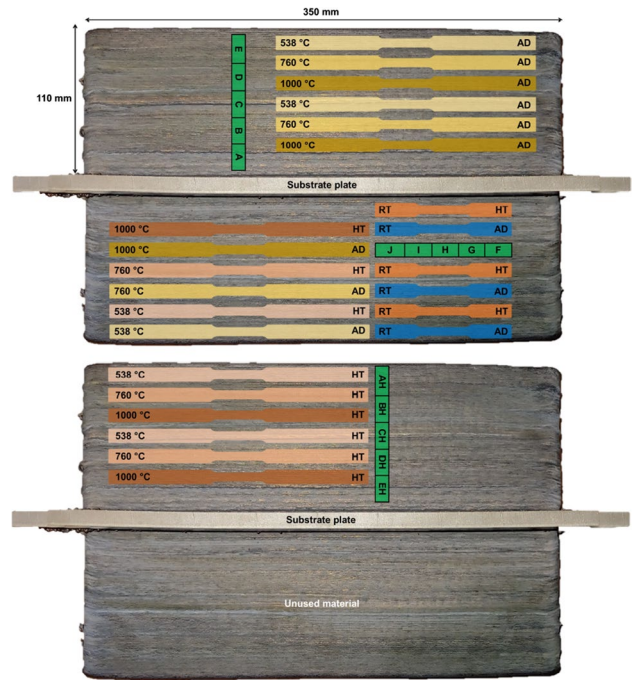


**Fig. 5** Location of extracted samples from WAAM walls. Green areas indicate the location of metallographic samples. Temperature given on the left of the coupon indicates testing temperature and on the right the condition AD or HT. Metallographic samples AH-EH are HT whereas single letters A-J are AD

orientations shown in Fig. 5. The room temperature (RT) coupon, conforming to ASTM E8(M) sub-size specification, is shown in Fig. 3, and the elevated temperature

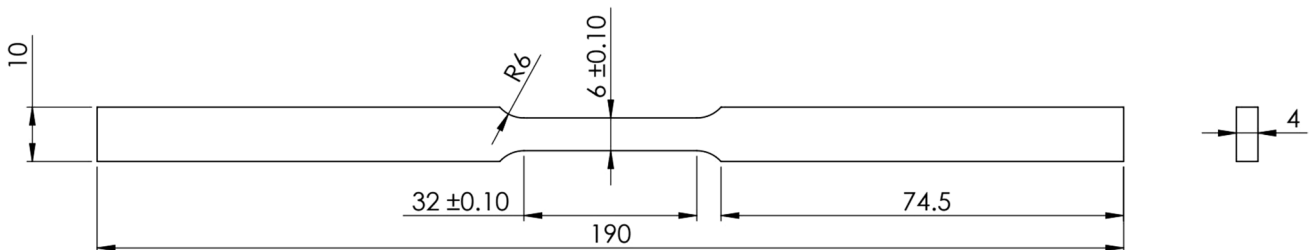


**Fig. 4** Elevated temperature testing coupon (dimensions in mm)

(538–1000 °C) coupon is shown in Fig. 4. Three coupons were tested in both AD and HT conditions at each temperature. Samples were tested at RT, 538, 760, and 1000 °C, using an Instron 8801 Servohydraulic Universal Testing System and tested to failure using ASTM E8(M) specification for RT testing and ASTM E21 for high-temperature testing. Tensile tests used a strain rate of  $0.005 \text{ min}^{-1}$  until the onset of plastic deformation and thereafter a crosshead speed of 1.6 mm/min. Prior to the start of testing, high-temperature specimens were held for 30 min at the testing temperature. Specimen

s were extracted from a variety of locations on the WAAM wall to minimise variation in results due to the WAAM aging effect. The fracture surfaces were carefully preserved for analysis.

The alloys in both AD and HT conditions also underwent microhardness testing using a Zwick/Roell hardness tester under a load of 500 g and holding time of 15 s. Several points were measured along a cross-section of material in both conditions to obtain an average value.

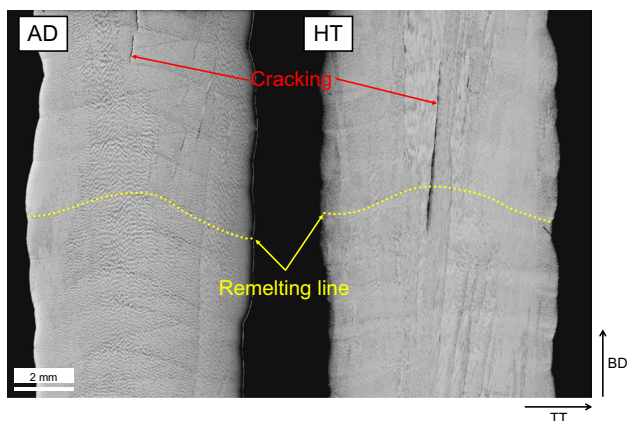
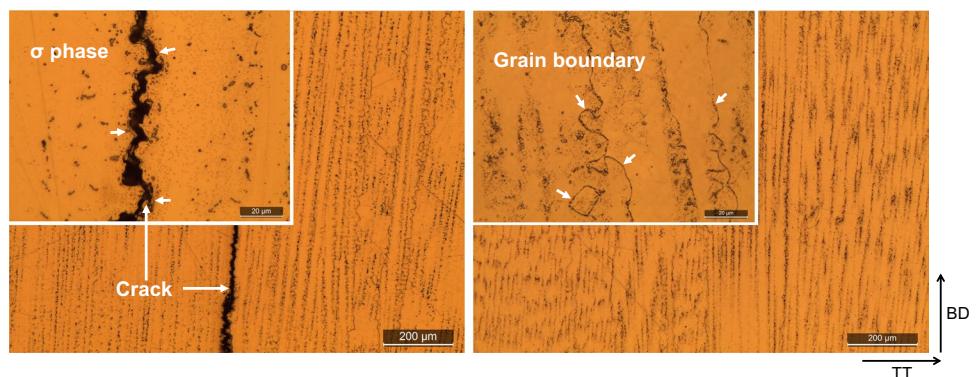


Fig. 6 AD [4] and HT macrostructure

Fig. 7 AD (left) and HT (right) optical observations



## 3 Results

### 3.1 Macrostructure

The macrostructure exhibits a typical solidified dendritic structure made up of large columnar grains which appear to extend along the BD from bottom to top. The macrostructure presented in Fig. 6 includes the AD macrostructure previously observed by James et al. [4] compared with the HT microstructure. The ripples of the successive welded layers are also observed and appear to have no effect on the grain structure. Several cracks were observed in the structure at the macro level. This grain structure was expected and is similar to that of IN718 seen in a previous study by Seow et al. [15]; there is little difference in the observed macrostructure, although HT specimens show a greater susceptibility to the etchant.

### 3.2 Microstructure

The microstructure was analysed both optically and under SEM. Optical images of the microstructure at comparable locations in both the AD and HT conditions are presented in Fig. 7. It can be clearly seen that the grain structure is similar in appearance, with long dendrites extending through the height of the samples in the BD axis. Grain boundary locations are shown for both samples, with the AD images displaying an intergranular crack. The micrographs show the directionally solidified grain structure, where the HT samples show a thicker dendritic structure and darker grain boundaries. A comparison at greater magnification in Fig. 7 is given in the top left of the micrographs. Precipitates can be seen at the crack edges in Fig. 7. Phases and carbides in this section going forward have been identified based on EDS composition and appearance using *ASM Atlas of Microstructures* [16]. It becomes clearer at greater magnification the thicker and darker grain boundaries after heat treating.

In HT samples of RE41 (Fig. 7), the grain boundary area presented is seen to consist of lighter coloured stringer-type

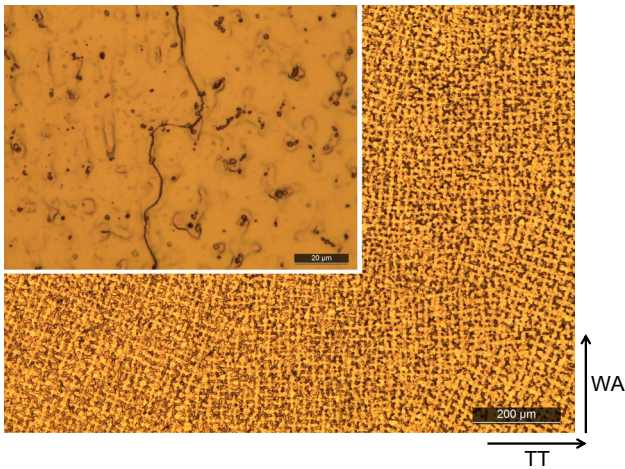
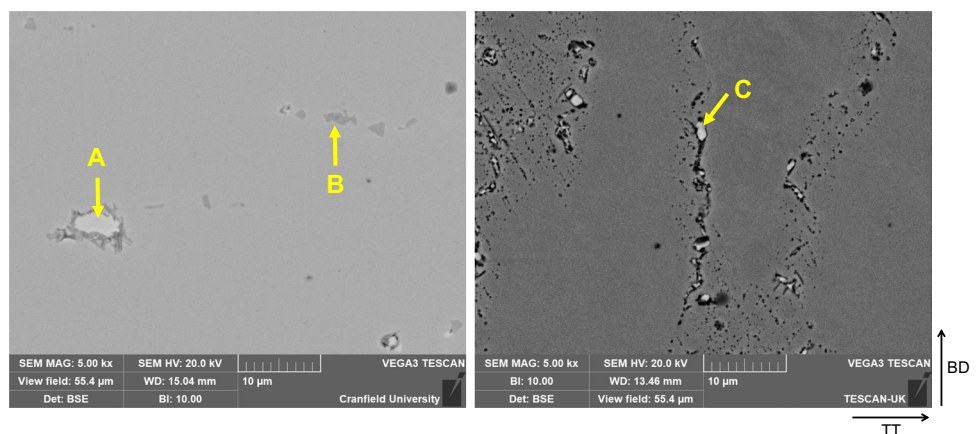


**Fig. 8** AD microstructure viewed in transverse (WA-TT) plane, showing cellular dendritic structure and precipitates in the interdendritic regions

precipitates, measuring  $0.5 \mu\text{m}$ , surrounded by a darker grain-boundary background, with larger, irregular-shaped grey precipitates, measuring mostly  $1\text{--}4 \mu\text{m}$ , distributed in the matrix. The lighter coloured precipitates at the grain boundary are thought to be carbides, while the grain boundaries are darkened in HT condition likely due to precipitation of  $\gamma'$ . The larger white, irregular-shaped precipitates, seen mostly at the grain boundaries, are thought to be a complex intermetallic phase. These phases can be observed in the HT sample in Figs. 7 and 8, but are more easily observed under SEM in Fig. 9.

When viewed in the transverse plane (WA-TT) in Fig. 8, a typical dendritic structure is apparent, with precipitates of  $1\text{--}2 \mu\text{m}$  seen mostly in the interdendritic regions. Also seen in Fig. 8 is a darkened grain boundary consistent with the HT material seen in image HT 2 (Fig. 7) although the precipitates along the grain boundary in AD material appear finer, which suggests the precipitates are carbides.

**Fig. 9** BSE images of AD (left) and HT (right) samples

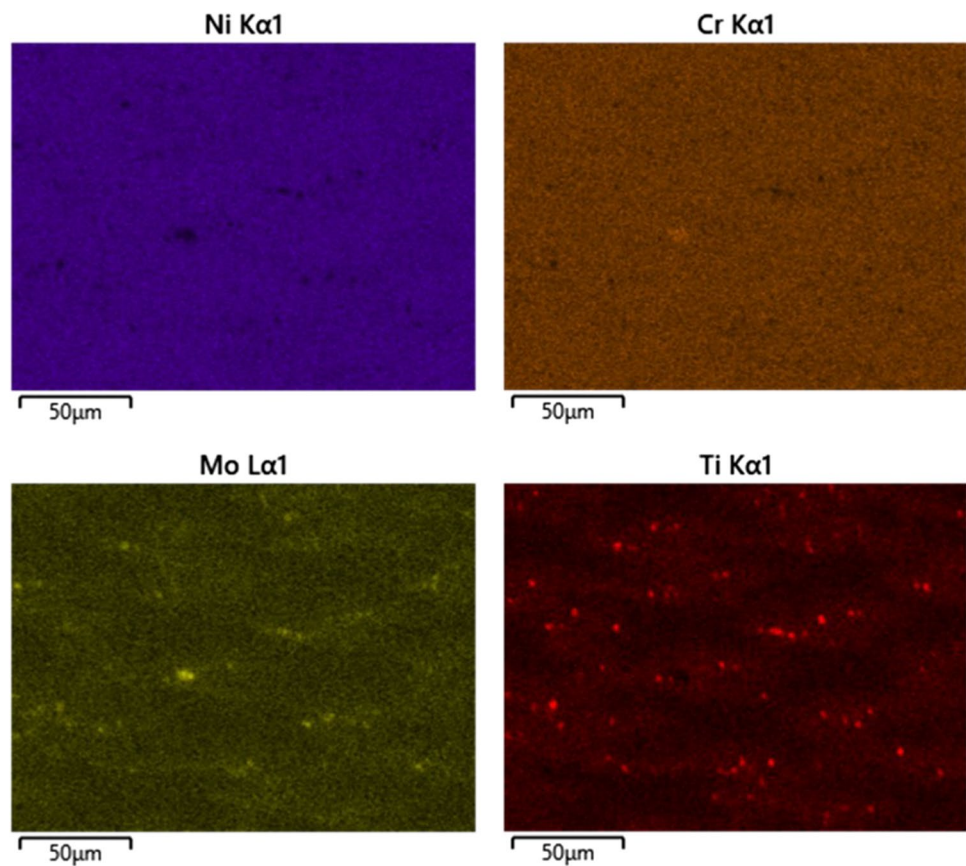


The AD WAAM structure shows significant amounts of segregation of Mo at Ti throughout the matrix, as seen in the elemental maps (Fig. 10). The segregation of Mo can be seen clearly, which corresponds to the lighter coloured phases in the BSE images; in these areas, Ni is depleted but Cr is not, indicating possible  $\sigma$  intermetallic phase (CrNiMo), which is supported by spectrum A in Table 2.

The darker grey coloured phases correspond to areas rich in Ti. These smaller Ti-rich zones were analysed using TOFSIMS to detect the presence of Ti and specifically C, which is less reliably indicated using EDS. In these areas, C and Ti were detected where Ni and Cr were shown to be depleted, indicating the presence of Ti-rich carbides, most likely TiC. Elemental maps of these areas are shown in Fig. 11 for AD material and correspond to the smaller grey-coloured precipitates seen in the matrix, labelled as B in Fig. 9 with EDS composition in Table 2. HT material was also analysed using the TOFSIMS facility, which identified similar formations of Ti-rich zones, corresponding to areas with higher concentrations of C. The HT material appears to have much larger precipitate formations, as well as detecting Al-rich precipitates. The carbide formations seen in HT material could be  $M_{23}C_6$  where M is a combination of Ti and Al which was also observed by Franklin and Savage [17] Fig. 12.

### 3.3 Dilution of IN718 substrate into RE41

As stated in Sect. 2.1, the deposition process utilised an IN718 substrate plate. It is necessary to examine the dilution of IN718 into the RE41 WAAM wall to determine how the composition of the WAAM material might be affected by using a different Ni-based alloy as a substrate. To determine the extent of dilution of IN718 into the RE41 matrix, elements which are not common between the two alloys were analysed, Fe forms  $18.5\% \text{wt}$  of IN718 and  $2.72\% \text{wt}$  of the RE41 wire, whereas Co forms  $10.2\% \text{wt}$  in RE41 and is not present in IN718. The line scan results shown in Fig. 13

**Fig. 10** EDS elemental map of AD material**Table 2** EDS analysis of areas marked in Fig. 9 (%at)

Spectrum label	Al	Ti	Cr	Fe	Co	Ni	Mo
A		1.55	34.16		10.86	30.26	23.17
B		15.61	22.21			62.18	
C	1.77	4.35	22.86	2.53	9.94	39.79	18.26

show how the level of Fe and Co changes with distance from the substrate. It can be seen that the level of Fe stabilises after approx. 2.1 mm. Co levels begin to stabilise after 1.2 mm increasing slightly until 2.1 mm beyond which remains relatively stable. To avoid any doubt in the reliability of mechanical results, samples were extracted more than 10 mm from the substrate.

### 3.4 Mechanical testing

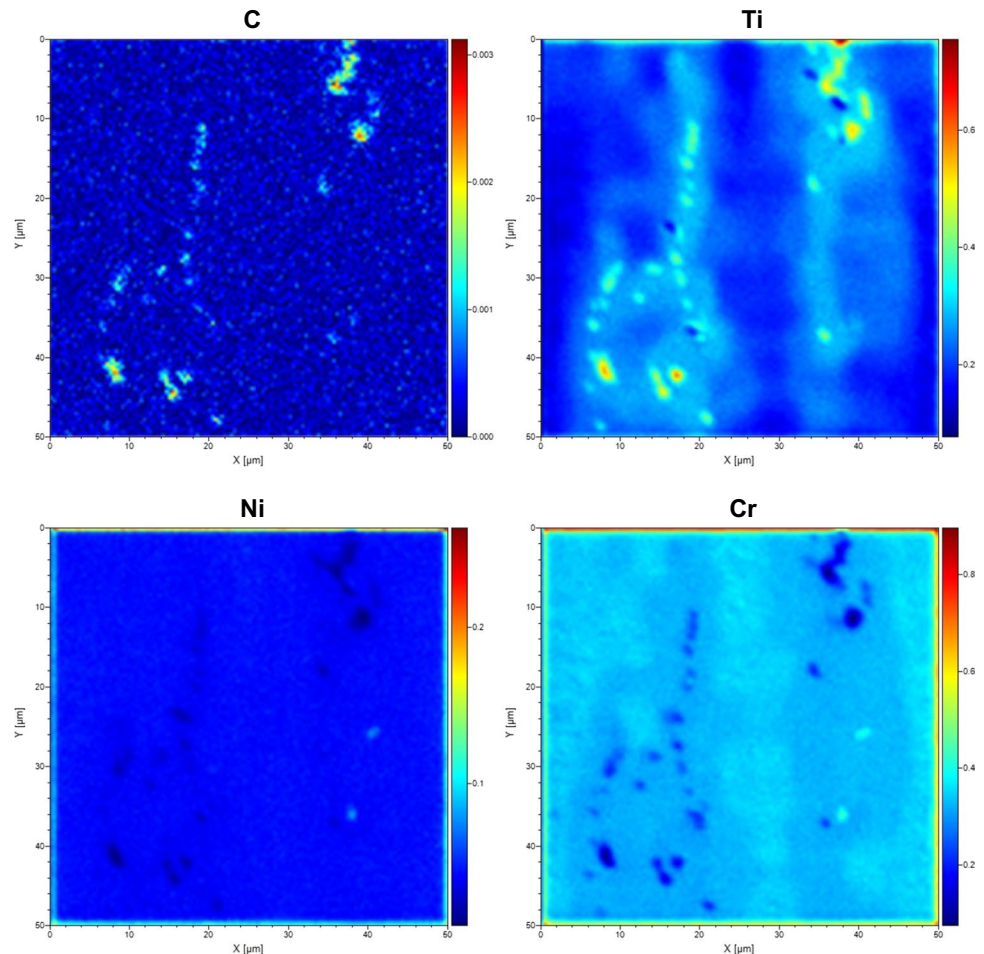
The results of tensile testing are given in Table 3, where wrought (Wro) values from the superalloy book by Donachie and Donachie [18] are presented alongside results for AD and HT samples. The data shows that even after heat treating, the WAAM material has not regained its wrought strength.

Graphs comparing the performance across the range of temperatures are shown in Fig. 14. An increase in performance was observed in the AD material during the 760 °C test and affected an increase in the performance compared with the 538 °C test which was unexpected. The AD material achieved an average of 58.8% of the wrought maximum, and when heat treated, the performance increases to an average of 61.4%.

Wrought RT hardness is provided in the manufacturer's data sheet as a minimum of 363 HV [19]. When tested, the AD and HT material had an average hardness of 410 HV and 497 HV respectively. The reason that there is an increase in hardness after heat treating is due to RE41 being precipitation strengthened.

It should be noted that unlike other alloying systems, the elastic modulus of Ni-based alloys is dependent on composition. As discussed by Parveen and Murthy, the

**Fig. 11** TOFSIMS elemental maps of AD material, showing potential carbides in areas rich in Ti and C, with depletion of Ni and Cr



elastic modulus is sensitive to minor changes in chemical composition that occur during heat treatment [20]. By extension, this could also apply to AD samples due to the partial aging effect which was observed by Xu et al. in WAAM built maraging steel [21].

### 3.5 Fracture surfaces

In the macrographs, most of the fracture surfaces have a woody appearance, indicating a shearing action across the grain plane which has produced cracking along many parallel longitudinal planes; further to this, most samples failed on an inclined plane also suggesting a shearing action. The woody appearance suggests that most fractures seen here are intergranular; a good example of this is seen in Fig. 15 image HT 1 that shows the surface of which is fibrous. On several samples, the lines sometimes take a chevron shape; these are theorised to be slip steps, although similar in appearance to striations which occur microscopically. Chevron patterns appear on mostly RT, 538 °C, and to a lesser extent 760 °C specimens; these patterns are indicative of rapid fracture associated with more brittle fractures, as seen in the ASM fractography atlas [23].

On 1000 °C specimens, the fractures appear more ductile in nature with distorted cross-sections. Specimens appear to have deep central void-type cracks which extend a good distance into the length of each specimen, suggesting much larger intergranular separation. The fracture surface of the 760 °C specimen appears far rougher and woodier in appearance. Fracture surfaces at this temperature appear to have areas seen as blue in colour, this perhaps indicates the formation of an oxide scale at this temperature, as samples were tested in air.

In Fig. 16, the microstructure 3 mm directly behind the fracture surface is shown for both conditions at each testing temperature. The grain boundaries appear to grow thicker with increased testing temperature; the difference is most noticeable in comparing the 1000 °C sample to the other temperatures (images AD 7 and AD 8). The grain boundaries are also noticeably thicker and more pronounced in HT specimens.

When looking at the features present 3 mm behind the fracture surfaces of specimens tested at 760 and 1000 °C (Fig. 17), differences were observed. The 760 °C specimen presents two distinct phases, of which one is bright in colour



and is rich in the alloying elements Cr, Ni, and Mo (spectrum A, Table 4) and is consistent with the appearance of the  $\sigma$  intermetallic phase (CrNiMo).  $\sigma$  phase is formed with exposure between 540 and 980 °C; it is seen to be irregularly shaped in the atlas of microstructures [16] and was also observed by Donachie and Donachie in Ni-Co alloys [10]. The second phase present (indicated by green arrows in Fig. 17) is rich in Ti (spectrum B, Table 4) and suggests the presence of carbide formation, likely TiC. A secondary crack is shown for the 1000 °C tested specimen. There appears to be, based on initial appearance,  $\delta$  phase precipitates (indicated by red arrows and C in Fig. 17). However, this is not the case, but on closer inspection using EDS analysis (Table 4), they appear to be entrapped oxide, which retain a good distribution of the alloying elements. This differentiates them from precipitates labelled D which is seen as the bright irregular-shaped areas central to the crack and forming along the crack edges, which is consistent with possible  $\sigma$  phase (CrNiMo).

When the fracture surfaces were examined microscopically in AD samples tested at RT and 760 °C (Fig. 18), the fracture surface exhibits a stepped surface with some evidence of beach marks in RT specimens which, although commonly associated with fatigue crack propagation, can be evidence of brittle fracture modes. Secondary cracking was observed in 760 °C specimens which showed an oxidised fracture surface.

## 4 Discussion

### 4.1 Macro- and microstructure

The macrostructure seen in RE41 is similar in appearance to that of IN718 observed by Seow et al. in an AD WAAM material. Large columnar grains extending through the BD axis, which extend outward with the flow of heat in the material in IN718, were also observed [15]. The appearance in RE41 of this effect is also noticeable, and it is likely that the same heat flux influenced grain structure seen by Wang et al. [24] is also occurring in WAAM built RE41.

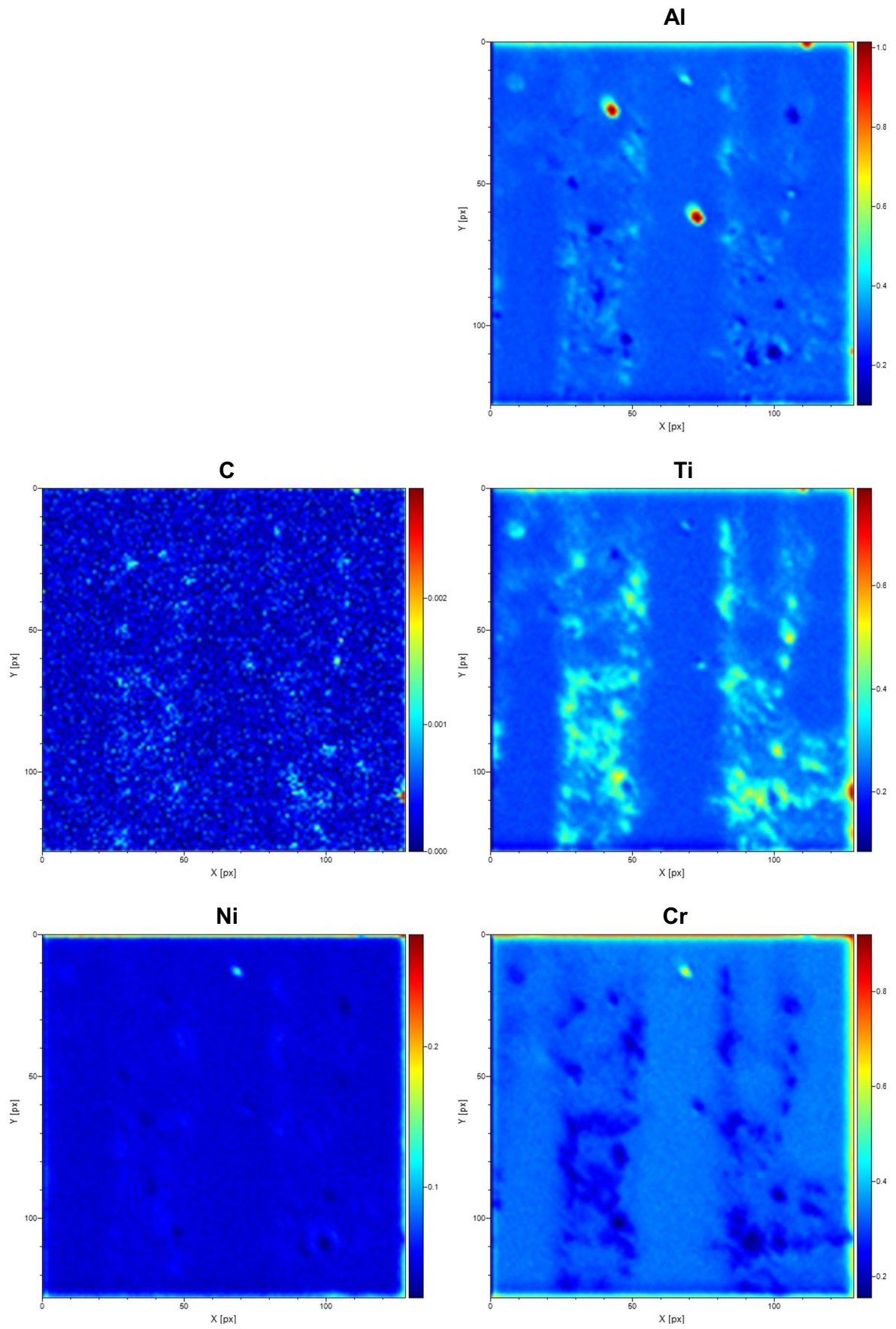
The comparison in Fig. 7 between AD and HT samples is especially interesting. The microstructure is similar in appearance to that which Li and Wang observed in their study of LMD of RE41 [8]. They observed the same epitaxial growth of the dendritic structure along the heat flux direction that was observed in this study. When the microstructure of HT RE41 is viewed optically, there are clear stringer like precipitates at the intergranular regions surrounded by a darker background which became more pronounced after heat treating, best seen in Fig. 7. Further investigation into literature suggested that these precipitates are likely to be MC,  $M_6C$ , or  $M_{23}C_6$  carbides while the darker background

is indicative of  $\gamma'$  precipitation, as seen in the microstructures atlas [16], which is expected post-aging. Franklin and Savage found that grain boundary carbides in RE41 form as  $M_6C$  type in solution annealed material and  $M_{23}C_6$  in over-aged material [17]. These precipitates, which appear darker grey in colour on the BSE images (Fig. 9), are thought to be Ti-rich carbides. This is supported by the EDS analysis of spectrum B in Table 2. The TOFSIMS analysis (Fig. 11) further indicates the presents of carbides by confirming the presence of C in these precipitates and the depletion of Ni and Cr. The larger white precipitates seen most clearly in image (Fig. 9), are thought to be  $\sigma$  intermetallic phase (CrNiMo) which is further supported by the EDS analysis in Table 2 spectrum A. These phases are also seen in HT samples, indicating that the standard 1065 °C solutionising treatment is not sufficient to dissolve these intermetallic top phases.

When the microstructure is viewed in the transverse (WATT) plane (Fig. 8), the dendritic structure is more apparent and is similar to the LMD microstructure observed by Li and Wang [8]; however, the cellular-dendritic structure observed in the WAAM material shows a more pronounced formation of secondary dendrite arms, and the precipitates forming in the interdendritic area are smaller with sizes of 1–2  $\mu\text{m}$ . Precipitates forming at the grain boundary in AD material appear finer than was observed in HT samples, which is indicative of carbide formation, most likely  $M_{23}C_6$  during heat treatment which was observed by Franklin and Savage, who found that a network of  $M_{23}C_6$  carbides forming in intergranular locations can be a cause of cracking in RE41 [17].

### 4.2 Effect of microstructure on mechanical performance

In the tensile results from RT–760 °C, a significant difference is observed in the performance of both variants of WAAM material and their stated maximum values from literature. Comparing UTS values, the HT specimens achieve roughly 67, 54, and 64% of their stated maximum at RT, 538, and 760 °C respectively. This difference was also observed in a previous study on IN718 by Xu et al. in which wrought IN718 was compared with WAAM material. The study showed that WAAM IN718 had a grain structure of far greater thickness and less grain boundary area than the wrought material. The strength of the wrought material is gained through its finer equiaxed grain structure and smaller dendrite arm spacing, allowing for more effective strengthening by precipitation of secondary phases at the grain boundaries. The larger columnar grains seen in the WAAM material made precipitation of these phases less likely. In this study, large columnar grains in RE41 also appear to have affected the strength in a similar way. A very similar



◀**Fig. 12** TOFSIMS elemental maps of HT material, showing potential carbides in areas rich in Ti with increased levels of Al and C

mismatch between HT WAAM specimens at the wrought strength was seen in Xu et al.'s study on IN718, which went further to examine the effect of differing heat treatments and found that unless a mechanical process was used to produce a more favourable starting microstructure, little to no additional enhancement in performance can be made [25].

An increase was also observed in the UTS and YS performance of the AD specimens when tested at 760 °C, which appear to have undergone aging during testing to 'catch-up' to the HT specimens, which was an intriguing finding. This finding is consistent with the microstructure observed in tested specimens (Fig. 16), where a clear darkening effect was observed around precipitates as the testing temperature was increased. The result of the increased stress performance is consistent with the results of Franklin and Savage when they examined the stress relaxation effect with temperature in RE41; they found that when tested at 760 °C the alloy precipitates larger  $\gamma'$  particles and also precipitates  $M_{23}C_6$  carbides in a continuous network at the grain boundaries,

resulting in increased stress but also results in greater levels of grain boundary cracking [17].

At 1000 °C, there was a sharp decrease in the performance, which is consistent with what was expected to be seen if the literature data is extrapolated to this temperature. Excessive blackening and oxidation cracking were observed on the 1000 °C samples post testing and is consistent with the findings of Greene and Finfrock with IN718, who found that at temperatures of 1000+ °C, volatile  $Cr_2O_3$  forms and results in the loss of the protective Chromia scale [26]. As the samples were tested in air at all temperatures, it is reasonable to assume that RE41 underwent this loss of protection, contributing to the performance reduction. The results from Collins and Quigg indicate that at temperatures around 900 °C,  $M_{23}C_6$  carbides dissolve leaving the grain boundaries free of precipitates [14], which would explain why the elastic modulus and mechanical performance were significantly reduced and the reason for the ductile behaviour when tested.

Very promising results were obtained for the reversal of strength loss at temperature, particularly for AD samples which close the gap in performance compared to HT samples at increased temperature. The findings help to understand the

**Fig. 13** Dilution of Fe and Co at substrate interface

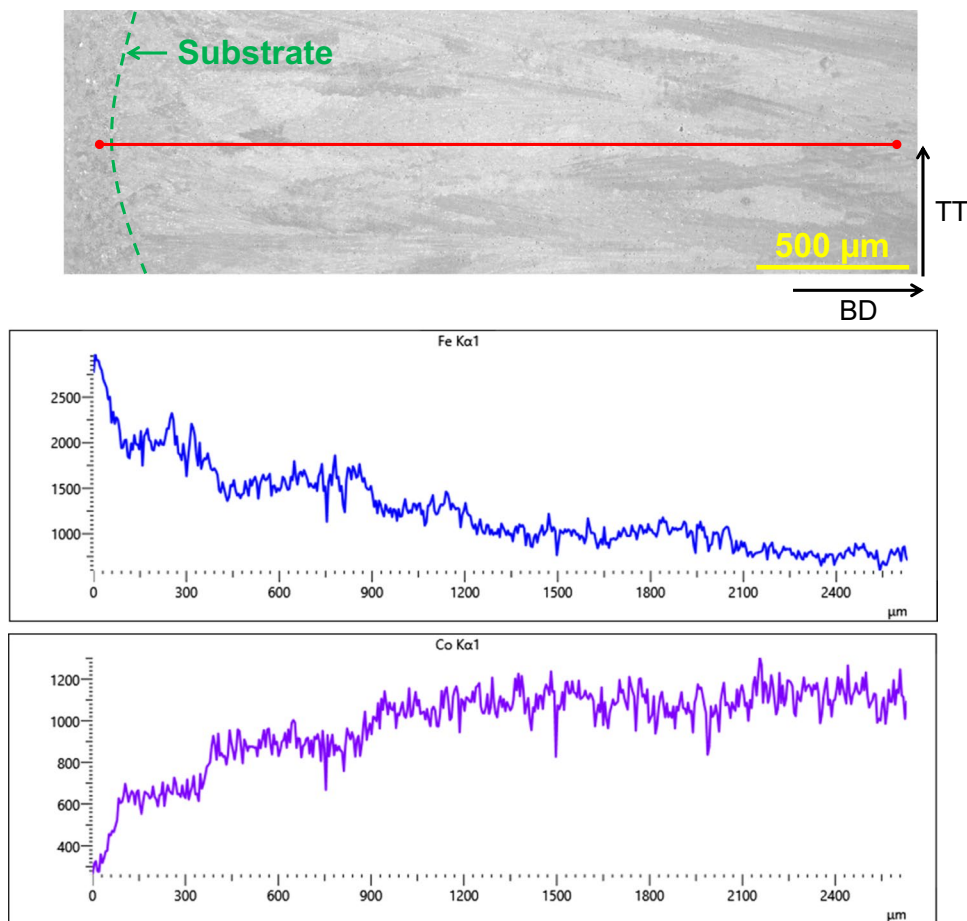


**Table 3** Tensile results [22] comparing wrought data (Wro) [18] with AD and HT material from RT-1000 °C

Temperature (°C)	UTS (MPa)			0.2% YS (MPa)			Elastic modulus <i>E</i> (GPa)			Tensile elongation (%)		
	Wro	AD	HT	Wro	AD	HT	Wro	AD	HT	Wro	AD	HT
RT	1420	855	945	1060	733	812	220	140	149	14	6.5	5.1
538	1400	703	757	1020	611	688	191	120	120	14	11.0	2.5
760	1105	728	704	940	669	671	173	103	107	11	3.8	1.4
1000		183	179		135	106		70	74		19.8	15.7

impact of matrix condition on mechanical properties at high temperatures. As the matrix structure of the AD and HT samples should be similar, it is interesting to observe AD sample age hardening during high-temperature testing. This aging process needs to be studied further to interpret the creep strength of RE41 and other such alloys at high temperatures. An investigation into precipitation kinetics would be vital to develop a fundamental understanding of precipitate evolution with temperature, and this would determine the suitability of an AD structure for high-temperature service.

It is interesting to observe the different performance at RT between samples extracted in the BD by James et al. and samples extracted along the WA in this study. James et al. found a RT UTS of 1017.4 MPa and a YS of 764.0 MPa for BD-oriented specimens [4], which performed approx. 19 and 4.2% higher than the performance of samples in this study, for UTS and YS respectively. The differing performance is thought to be due to the difference in orientation of the large columnar grain structure.

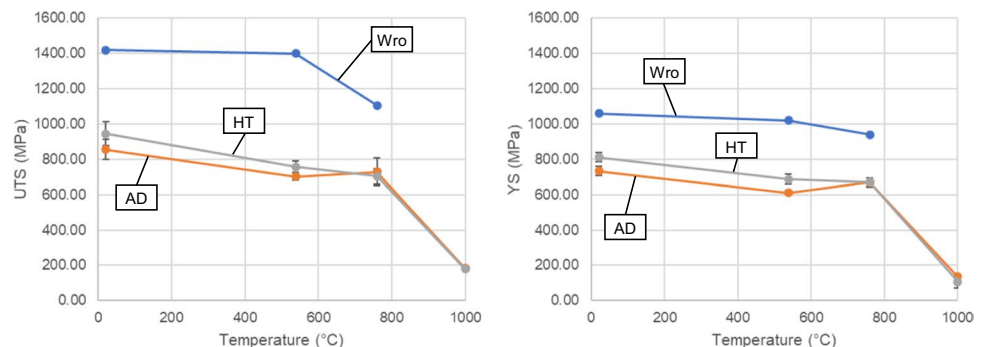
In general, the WAAM process is thought to partially age alloys in varying amounts dependent on the process used and the metallurgy of the alloy being deposited. This was observed in IN718 by Xu et al. who found that the hardness increase due to the WAAM process is also variable, dependent on the amount of successive heating cycles the material has been subjected to [3]. For example, the WAAM walls produced for this study had roughly the same number of deposited layers; for RE41, this was between 147 and 153 layers per wall, meaning roughly the same number of successive thermal cycles has occurred during the process.

However, only the very first layer has experienced all of these cycles, whereas the very last layer, i.e. the top of the WAAM wall, has only experienced one heating cycle. This means that the partial aging effect is more pronounced at the bottom of the WAAM wall, whereas the top of the wall is significantly less aged. This effect was investigated by Xu et al. in a study on maraging steel, in which it was found that the bottom part of the WAAM walls was harder than the top parts. Xu et al. found that the number of precipitates in the bottom part of AD walls was roughly double the number of precipitates found in the top part. With an aging treatment however, the precipitates in the top part of the wall increased to be approximately the same as the bottom part [21]. The location of AD samples extracted for hardness testing in this study was in the centre of each wall, where the WAAM aging effect is roughly half the number of deposited layers.

### 4.3 Fractography

With the largely different performance of AD samples at 760 °C and the suggestion that these samples appear to undergo aging during testing to ‘catch-up’ to the pre-HT duplicate, it was not surprising to see that the macrofractography shows a visible difference in the fracture surfaces at this temperature. The surface of the fractures appears blue in colour. This is useful evidence for the theory that the alloy has undergone a change during testing at 760 °C, which is not entirely surprising given that RE41 is routinely aged around this temperature. What is surprising is the change in appearance even on the

**Fig. 14** Graphical representation of data presented in Table 3. UTS (left) and YS (right)



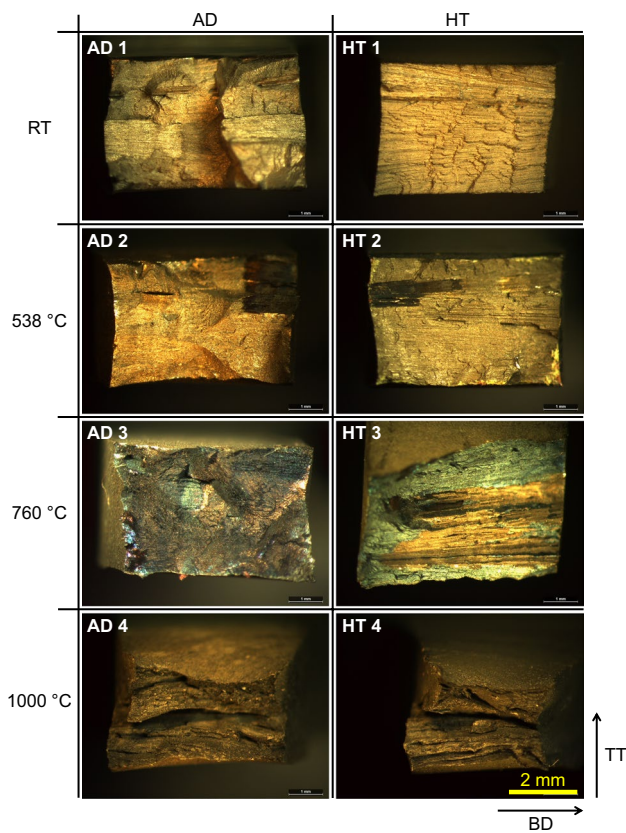


Fig. 15 AD and HT macrofractographic images of fracture surfaces

macroscale which suggests that this is merely the appearance of an oxide formation.

The fracture surfaces of specimens tested at 1000 °C suggest that fractures were very much ductile in nature, due to the distorted cross-sections and ‘hour-glass’ shape. The testing data also showed a clear reduction in elastic modulus of samples tested at this temperature. Again, this is consistent with the findings of Greene and Finrock on IN718, in which it was found that at temperatures of 1264 °C, not hugely removed from 1000 °C, the deformation in the alloy became unacceptable for the application [26]. It is also noticeable that with increasing testing temperature, the grain boundaries become much thicker. This was seen in RE41 by Schwartz et al. in a study where RE41 underwent heating cycles which affected the thickness of the grain boundaries and also the susceptibility to the metallographic etchant [11]; this was also observed in this study especially 1000 °C tested specimens (Fig. 16: image AD 8 & HT 8). Specimens tested at RT, 538, and to a lesser extent 760 °C showed signs of more brittle fractures, which is supported by the elongation data that shows only a fraction of the elongation expected compared with wrought data. Furthermore, chevron patterns seen in these specimens add to evidence of brittle-type

fractures, as the fractography handbook suggests they are indicative of more rapid fracture modes [23].

In Fig. 17, oxide formation at the grain boundaries of RE41 tested at 1000 °C was observed, and the oxide takes a similar shape to that of the  $\delta$  phase commonly seen in IN718, with its acicular needle-like shape and its formation in close proximity to potential intermetallic phases; however, this is not possible in RE41 due to the lack of Nb needed for its precipitation. Upon investigating the composition using EDS, it was found that the composition retains the distribution of the alloying elements; however, it shows an increase in the amount of detected O. This is consistent with the finding of Ungureanu et al. In their study, RE41 underwent a thermal shock process to understand the effects on the microstructure; at 1000 °C, it was found that with increased thermal shock, oxide layers were seen to grow and retain a similar distribution of the alloying elements [27]. Ultimately, the formation of oxide in the samples is consistent with the tensile results, as the elongation of the samples represents only a fraction of the expected elongation from wrought material, indicating that the presence of oxide has affected the ductility of the alloy. Entrapped oxides

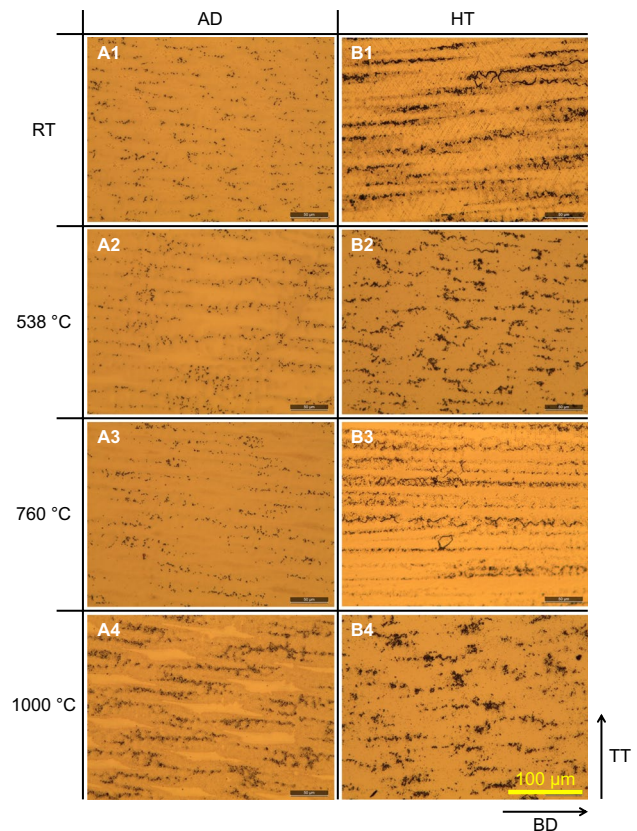
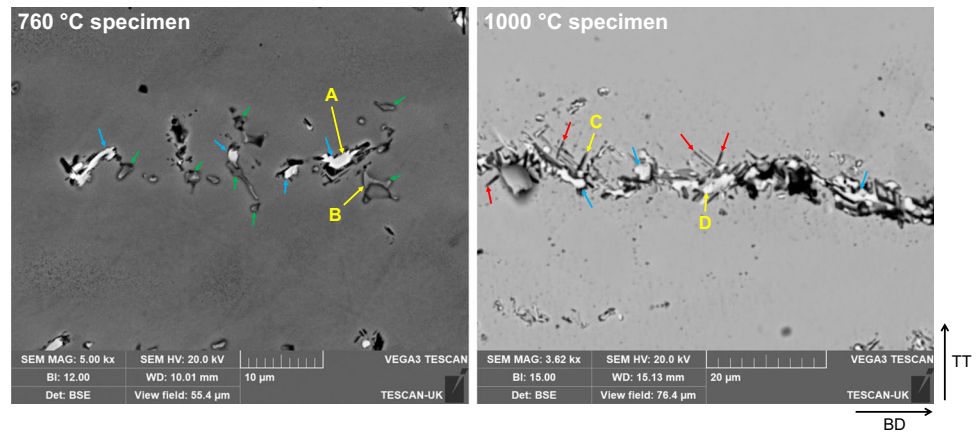


Fig. 16 Microstructure of AD & HT tensile specimens directly behind fracture surface

**Fig. 17** BSE images behind fracture surface: 760 °C tested specimen (left); 1000 °C tested specimen (right). Green arrows indicate Ti-rich potential MC carbides, blue arrows indicate  $\sigma$  phase, and red arrows indicate oxide formation



**Table 4** EDS analysis of areas marked in Fig. 17 (%at)

Label	O	Al	Si	Ti	Cr	Fe	Co	Ni	Mo	Possible phase
A		1.17		2.18	33.29	2.39	10.36	29.22	21.25	$\sigma$ (CrNiMo)
B		3.13		15.16	18.68	2.09	7.95	41.89	10.87	MC (TiC)
C	9.13	2.85	2.57	3.56	19.74	2.66	9.12	45.34	5.04	Oxide
D	13.17	1.23	1.73	4.40	20.76	1.73	8.16	28.58	20.25	$\sigma$ (CrNiMo)

formed during the welding process would not be possible to dissolve into the matrix during solutionising, due to their extremely high melting point. The low viscosity of Ni alloys makes them particularly susceptible to oxide entrapment, which is also consistent with the findings of Xu et al. in their study on maraging steel, in which oxides were also found to have a strengthening effect on the matrix when dispersed on the hundred-nanometre scale [28]. It appears that controlling the oxygen level below 800 ppm during deposition was not sufficient to prevent oxidation. In future studies, the level should therefore be controlled to a lower concentration to prevent oxide entrapment. Microscopically, in Fig. 18, fracture surfaces generally exhibited a local stepwise method of fracture with signs of brittle fracture at RT, and secondary cracking was observed at increased testing temperature where fracture surfaces were also oxidised.

#### 4.4 High-speed flight application

In reference to the introduction of this paper, the intended application of this research is in understanding the high-temperature performance of RE41, for highly stressed service in temperatures of 1000 + K for durations of < 1 h.

In terms of tensile performance, RE41 achieves high stress values at most tested temperatures. However, toward the 1000 °C testing temperature, the performance of RE41 decreases somewhat exponentially, illustrating that

the alloy has a much better performance definitively at temperatures < 1000 °C.

Elastic modulus is another important factor for high-speed flight applications, as components need to retain their shape at service temperatures; a lower deformation during loading is therefore preferred. However, alloys need to retain some ductility to avoid the devastating impacts of brittle-type fractures during service. RE41 showed only a fraction of the expected elastic modulus from wrought material. The majority of fractures were brittle in nature; however, with increasing temperature the fracture mode tends toward more ductile fractures, with the noted exception of the 760 °C test.

A small amount of intergranular cracking was observed in both AD and HT materials. It is hoped that a further mechanical process introduced during WAAM deposition will help to alleviate the cracking issues through the relief of residual strain induced by the process. This will be the subject of a future study.

## 5 Conclusion

1. AD WAAM RE41 achieves 58.8% of the maximum wrought performance. Heat-treating results in a performance increase to 61.4% and in the alloy being 37% harder than the minimum wrought values.
2. When tested at 760 °C, the performance of AD precipitation-strengthened alloys increases to meet the perfor-

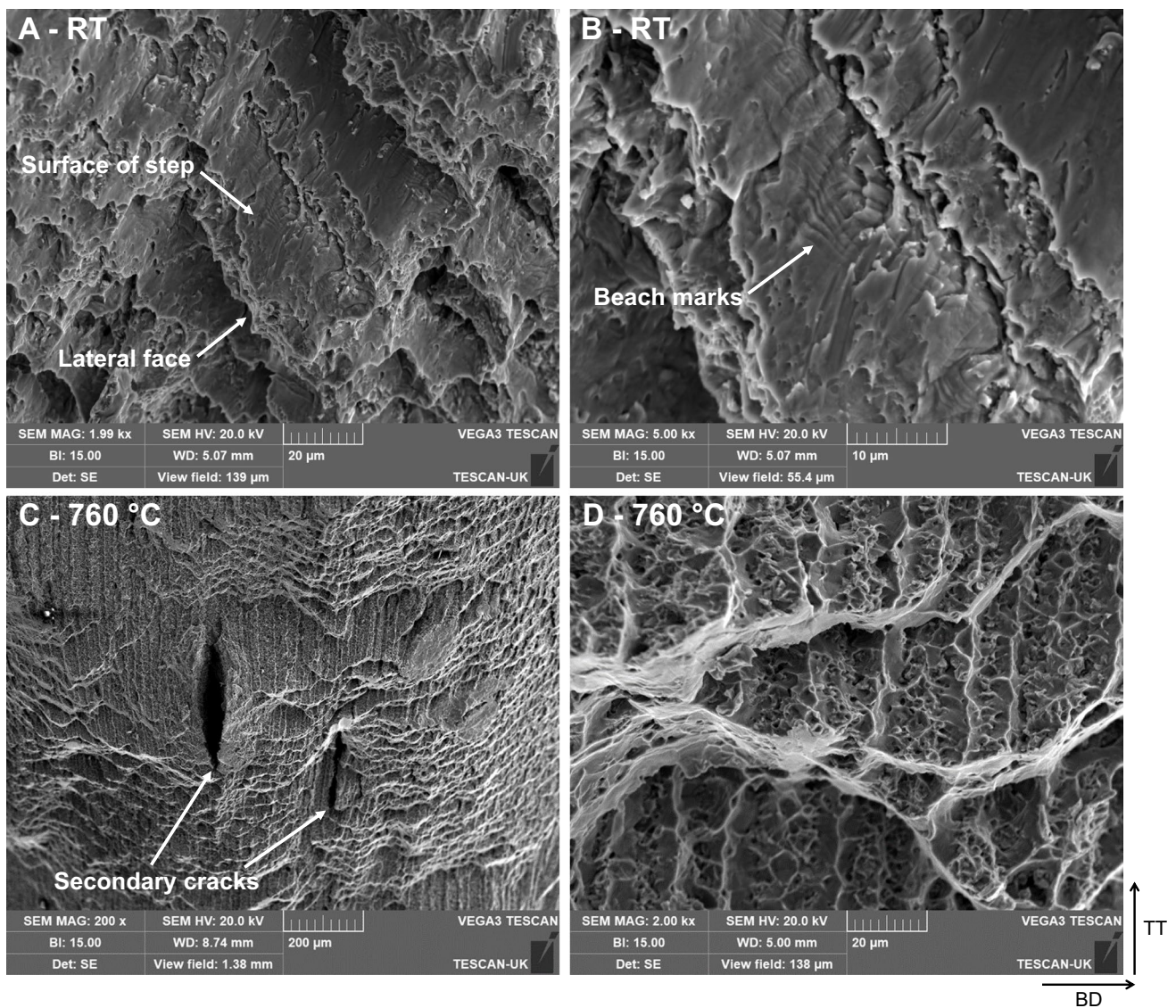


**Fig. 18** Fractography of AD material tested at RT (top) and 760 °C (bottom). Images show stepwise fracture surface. Image B shows beach marks on step surface. Image C shows secondary cracks and D the oxidation on the fracture surface

mance of pre-HT specimens, indicating an in-test aging process.

3. Subjecting RE41 to the standard heat treatment post-deposition causes the hardness to increase above the minimum wrought values, which is likely due to the formation of potential tcp phases during heat treatment, as a result of the segregation of heavier elements during deposition.
4. Performance and elastic modulus reduce at a 1000 °C testing temperature, potentially due to the dissolution of carbides and presence of undesirable oxide phases at the grain boundaries.
5. The formation of carbide networks and potential intermetallic phases at the grain boundaries are responsible

for intergranular cracking observed in both AD and HT material.

6. A solutionising temperature of 1065 °C is not sufficient to dissolve undesirable potential tcp phases in WAAM built RE41.
7. There is a small dilution of the IN718 substrate into the RE41 deposition. This could vary depending upon the deposition parameters and should be accounted for when building dissimilar AM/substrate structures.
8. WAAM built RE41 requires additional investigation to increase performance to wrought values and to make the WAAM built material suited to high-speed flight applications.

**Acknowledgements** The authors wish to acknowledge the industrial supervisors from DSTL Porton Down, for their ongoing advice and guidance: Graham Simpson and Dr Matthew Lunt. The authors would also like to acknowledge the technical assistance from Tracey Roberts, Steve Pope, and Kristopher Bramley during imaging.

**Funding** The authors wish to acknowledge the UK Ministry of Defence for their financial support. This work was funded by the Defence Science & Technology Laboratory, UK (DSTL).

**Data availability** The raw data required to reproduce these findings are available to download from <https://doi.org/10.17862/cranfield.rd.20142737>. The processed data required to reproduce these findings are available to download from <https://doi.org/10.17862/cranfield.rd.20142086>.

**Code availability** Not applicable.

## Declarations

**Ethics approval** In the author's opinion, there are no ethical issues with the research presented in this paper.

**Consent to participate** Not applicable.

**Consent for publication** All authors consent to the publication of this paper.

**Conflict of interest** The authors declare no conflict of interest.

**Open Access** This article is licensed under a Creative Commons Attribution 4.0 International License, which permits use, sharing, adaptation, distribution and reproduction in any medium or format, as long as you give appropriate credit to the original author(s) and the source, provide a link to the Creative Commons licence, and indicate if changes were made. The images or other third party material in this article are included in the article's Creative Commons licence, unless indicated otherwise in a credit line to the material. If material is not included in the article's Creative Commons licence and your intended use is not permitted by statutory regulation or exceeds the permitted use, you will need to obtain permission directly from the copyright holder. To view a copy of this licence, visit <http://creativecommons.org/licenses/by/4.0/>.

## References

- Williams SW, Martina F, Addison AC, Ding J, Pardal G, Colegrove P (2016) Wire + arc additive manufacturing. *Mater Sci Technol* 32:641–647. <https://doi.org/10.1179/1743284715Y.0000000073>
- Marinelli G, Martina F, Ganguly S, Williams S (2019) Development of Wire + arc additive manufacture for the production of large-scale unalloyed tungsten components. *Int J Refract Met Hard Mater* 82:329–335. <https://doi.org/10.1016/j.ijrmhm.2019.05.009>
- Xu X, Ganguly S, Ding J, Seow CE, Williams S (2018) Enhancing mechanical properties of wire + arc additively manufactured INCONEL 718 superalloy through in-process thermomechanical processing. *Mater Des* 160:1042–1051. <https://doi.org/10.1016/j.matdes.2018.10.038>
- James WS, Ganguly S, Pardal G (2022) Selection and performance of AM superalloys for high-speed flight environments. *Int J Adv Manuf Technol* 122:2319–2327. <https://doi.org/10.1007/s00170-022-10005-9>
- Battelle Memorial Institute, Heat-resistant alloys, in: *Met. Mater. Prop. Dev. Stand.*, Battelle Memorial Institute, 2017. <https://app.knovel.com/hotlink/pdf/id:kt00CX2NX1/metallic-materials-properties/metallic-m-mechanical>
- Wile GJ (1963) Superalloys for aerospace application. *Jom* 15:645–647. <https://doi.org/10.1007/bf03397242>
- Li J, Wang HM, Tang HB (2012) Effect of heat treatment on microstructure and mechanical properties of laser melting deposited Ni-base superalloy Rene'41. *Mater Sci Eng A* 550:97–102. <https://doi.org/10.1016/j.msea.2012.04.037>
- Li J, Wang HM (2010) Microstructure and mechanical properties of rapid directionally solidified Ni-base superalloy Rene'41 by laser melting deposition manufacturing. *Mater Sci Eng A* 527:4823–4829. <https://doi.org/10.1016/j.msea.2010.04.062>
- SE Atabay, O Sanchez-Mata, JA Muñiz-Lerma, R Gauvin, M Brochu (2020) Microstructure and mechanical properties of rene 41 alloy manufactured by laser powder bed fusion. *Mater Sci Eng A* 773 (2020) <https://doi.org/10.1016/j.msea.2019.138849>
- MJ Donachie, SJ Donachie (2002) Understanding superalloy metallurgy, in: *Superalloys - a tech. guid.*, 2nd ed., ASM International 25–39 <https://doi.org/10.31399/asm.tb.stg2.t61280025>
- Schwartz M, Ciocoiu R, Gheorghie D, Jula G, Ciucă I (2015) Preliminary research for using Rene 41 in confectioning extrusion dies. *Mater. Characterisation VII* 1:95–106. <https://doi.org/10.2495/mc150091>
- Kaufman M (1963) Control of phases and mechanical properties in nickel-base alloys of Rene 41 type. *Trans Metall Soc AIME* 227:405
- Weisenberg LA, Morris RJ (1960) How to fabricate Rene 41. *Met Prog* 78:70–74
- Collins HE, Quigg RJ (1968) Carbide and intermetallic instability in advanced nickel-base superalloys. *Am Soc Met Trans Q* 61:139–148
- Seow CE, Coules HE, Wu G, Khan RHU, Xu X, Williams S (2019) Wire + arc additively manufactured Inconel 718: effect of post-deposition heat treatments on microstructure and tensile properties. *Mater Des* 183:108157. <https://doi.org/10.1016/j.matdes.2019.108157>
- ASM Committee of Metallography of Heat-Resisting Alloys (1972) Microstructures of wrought heat-resisting alloys, in: *ASM met. handb. Vol. 7 Atlas microstruct. ind. alloy.*, 8th ed., ASM International 165–192
- J.E. Franklin, W.F. Savage, stress relaxation and strain-age cracking in Rene 41 weldments, *Weld. J.* 53 (1974) 380–387. [http://aws.perusion.com/wj/supplement/WJ\\_1974\\_09\\_s380.pdf](http://aws.perusion.com/wj/supplement/WJ_1974_09_s380.pdf)
- M.J. Donachie, S.J. Donachie, Selection of superalloys, in: *Superalloys - a tech. guid.*, 2nd ed., ASM International, 2002: pp. 11–24. <https://app.knovel.com/hotlink/pdf/id:kt008GQQU1/superalloys-technical/superalloy-forms>
- Rolled alloys, Data sheet Rene 41, (2011). <http://www.rolledalloys.com/alloys/cobalt-alloys/rene-41/en/>. Accessed 5 July 2022
- Parveen N, Murthy GVS (2011) Determination of elastic modulus in nickel alloy from ultrasonic measurements. *Bull Mater Sci* 34:323–326. <https://doi.org/10.1007/s12034-011-0070-z>
- Xu X, Ganguly S, Ding J, Guo S, Williams S, Martina F (2018) Microstructural evolution and mechanical properties of maraging steel produced by wire + arc additive manufacture process. *Mater Charact* 143:152–162. <https://doi.org/10.1016/j.matchar.2017.12.002>
- WS James, S Ganguly, G Pardal (2022) Rene 41 tensile data, Cranf. Online Res. Data. Dataset <https://doi.org/10.17862/cranfield.rd.20142737>
- ASM Handbook Committee (1987) Visual examination and light microscopy, in: G.F. Vander Voort (Ed.), *Fractography*, 8th ed., ASM International 91–165 <https://doi.org/10.31399/asm.hb.v12.a0001834>
- Wang JF, Sun QJ, Wang H, Liu JP, Feng JC (2016) Effect of location on microstructure and mechanical properties of additive layer manufactured Inconel 625 using gas tungsten arc welding. *Mater Sci Eng A* 676:395–405. <https://doi.org/10.1016/j.msea.2016.09.015>



25. Xu X, Ding J, Ganguly S, Williams S (2019) Investigation of process factors affecting mechanical properties of INCONEL 718 superalloy in wire + arc additive manufacture process. *J Mater Process Technol* 265:201–209. <https://doi.org/10.1016/j.jmatp.2018.10.023>
26. Greene GA, Finrock CC (2001) Oxidation of inconel 718 in air at high temperatures. *Oxid Met* 55:505–521. <https://doi.org/10.1023/a:1010359815550>
27. Ungureanu E, Anghel DC, Negrea D, Plaiu AG, Rizea V, Dicu MM, Ducu CM, Abrudeanu M (2019) Influence of thermal shocks at high temperatures on microstructure and hardness of RENE 41 alloy. *IOP Conf Ser Mater Sci Eng*. <https://doi.org/10.1088/1757-899X/564/1/012046>
28. Xu X, Ding J, Ganguly S, Diao C, Williams S (2018) Oxide accumulation effects on wire + arc layer-by-layer additive manufacture process. *J Mater Process Technol* 252:739–750. <https://doi.org/10.1016/j.jmatprotec.2017.10.030>

**Publisher's note** Springer Nature remains neutral with regard to jurisdictional claims in published maps and institutional affiliations.